results are compatible with this prediction. For $\mathbf{H} \perp b$ as well the observed slight intensity increase and the red shift of the high-energy peaks at $T = 1.9$ K, as the other magnetic field effects at $T \geq 10$ K (cf. Figure 10), may be caused by a small misalignment of the applied magnetic field, yielding an admixture of $\mathbf{H} \parallel b$ with the supposed $\mathbf{H} \perp b$ field.

Acknowledgment. This research has been supported by the Deutsche Forschungsgemeinschaft, the Fonds der Chemischen Industrie, and the Swiss National Science Foundation.

Contribution from the Department of Chemistry and Illinois ESR Research Center, University of Illinois at Urbana-Champaign, 505 South Mathews Avenue, Urbana, Illinois 61801

EPR-Derived Electronic Characteristics of Zerovalent Manganese Carbonyl Di(tertiary phosphine) Radicals

Gail B. Rattinger, R. Linn Belford,* Howard Walker, and T. L. Brown*

Received November 4, 1987

Persistent $Mn(CO)_3L_2$ metal-centered radicals, where the ligand, L, is either a tertiary phosphine or phosphite, are isoelectronic with the pentacyanocobaltate radical anion, $Co(CN)_5^{3-}$, a well-characterized radical,[6] and with the unsubstituted manganese(0) pentacarbonyl radical. This paper presents a characterization via multifrequency EPR spectroscopy of a series of $\cdot Mn(CO)_3L_2$ radicals—$\cdot Mn(CO)_3[P(n\text{-}Bu)_3]_2$, $\cdot Mn(CO)_3[P(i\text{-}Bu)_3]_2$, $\cdot Mn(CO)_3[P(i\text{-}Pr)_3]_2$, and $\cdot Mn(CO)_3[P(O\text{-}i\text{-}Pr)_3]_2$. Anisotropic g shifts and metal hyperfine and phosphorus superhyperfine spin Hamiltonian parameters are reported and compared to values reported in the literature for $\cdot Mn(CO)_5$. It is thus possible to examine some of the effects of varying ligand, geometry, and electronic parameters upon the characteristics of the EPR spectra obtained and upon the unpaired spin density localized in the manganese $3d_{z^2}$ and 4s metal orbitals and delocalized onto the phosphorus ligands. An LCAO–MO perturbation treatment of g and A values for these square-pyramidal d^7 systems yields reasonable estimates of the distribution of unpaired spin density, upper and lower limits of core polarization, and the energy difference, ΔE, between the ground state and $d\pi$ excited state.

Introduction

Interest in organometallic species has grown steadily over the last 40 years. Seventeen-electron (17e) organometallic free radicals and their reaction pathways have been of particular interest on account of their possible roles in homogeneous catalysis.[1-7] There have been numerous studies of the participation of metal-centered organometallic species in hydride abstraction,[8-10] electron transfers,[11-13] ligand substitutions,[4,8,13b,14-16] atom transfers,[3,9,17] and oxidative additions/reductive eliminations.[3,18] Because of rapid radical recombination it is difficult to prepare persistent zerovalent manganese-centered radicals; consequently, few examples are found in the literature.[9,10] Persistent $Mn(CO)_3L_2$ metal-centered radicals have been generated, where the ligand, L, is either a tertiary phosphine or phosphite.[9,10,19] These species are isoelectronic with the pentacyanocobaltate radical anion, $Co(CN)_5^{3-}$, a well-characterized radical,[6] and with the unsubstituted manganese(0) pentacarbonyl radical.[21,22] This paper presents a characterization via multifrequency EPR spectroscopy of a series of $\cdot Mn(CO)_3L_2$ radicals. We chose to study $\cdot Mn(CO)_3[P(n\text{-}Bu)_3]_2$, $\cdot Mn(CO)_3[P(i\text{-}Bu)_3]_2$, $\cdot Mn(CO)_3[P(i\text{-}Pr)_3]_2$, and $\cdot Mn(CO)_3[P(O\text{-}i\text{-}Pr)_3]_2$ in order to examine the effects of varying steric and electronic parameters[23,24] upon the characteristics of the EPR spectra obtained and upon the unpaired spin density localized in the manganese $3d_{z^2}$ and 4s metal orbitals and delocalized onto the phosphorus ligands. Anisotropic g shifts and metal hyperfine and phosphorus superhyperfine spin Hamiltonian parameters are reported and compared to values reported for $\cdot Mn(CO)_5$.[21] An LCAO–MO perturbation treatment of g and A values for these square-pyramidal d^7 systems yields reasonable estimates of the distribution of unpaired spin density, upper and lower limits of core polarization, and the energy difference, ΔE, between the ground state and $d\pi$ excited state. A less detailed study of $\cdot Mn(CO)_3L_2$ radicals has previously appeared.[25]

Experimental Section

All of the manganese radical samples were synthesized according to reported procedures.[9,10,19] The samples were transferred on a vacuum line directly into quartz EPR tubes, which were sealed for detachment to protect the air-sensitive radical. All of the samples were within a concentration range of 0.54–1.0 mM in hexane. The samples were then quickly frozen by immersion in liquid nitrogen and stored at 77 K. Useful lifetimes of samples kept in this way ranged from a few weeks to a maximum of 3 months. The quick freezing promoted good glassing,

(1) Brown, T. L. *Ann. N.Y. Acad. Sci.* **1980**, *330*, 80.
(2) Kochi, J. K. *J. Organomet. Chem.* **1986**, *300*, 139.
(3) (a) Wegman, R. W.; Brown, T. L. *Organometallics* **1982**, *1*, 47. (b) McCullen, S. B.; Brown, T. L. *Inorg. Chem.* **1981**, *20*, 3528.
(4) Forbus, N. P.; Brown, T. L. *Inorg. Chem.* **1981**, *20*, 4343.
(5) Kwiatek, J. *Catal. Rev.* **1967**, *1*, 37.
(6) Chock, P. B.; Dewar, R. B. K.; Halpern, J.; Wong, L. *J. Am. Chem. Soc.* **1969**, *91*, 82. Chock, P. B.; Halpern, J. *J. Am. Chem. Soc.* **1969**, *91*, 582.
(7) Lappert, M. F.; Lednor, P. W. *Adv. Organomet. Chem.* **1976**, *14*, 345.
(8) Byers, B. H.; Brown, T. L. *J. Am. Chem. Soc.* **1977**, *99*, 2527.
(9) McCullen, S. B.; Brown, T. L. *J. Am. Chem. Soc.* **1982**, *104*, 7496.
(10) Kidd, D. R.; Cheng, C. P.; Brown, T. L. *J. Am. Chem. Soc.* **1978**, *100*, 4103.
(11) (a) Kochi, J. K. *Acc. Chem. Res.* **1974**, *7*, 351. (b) Kochi, J. K. *Organometallic Mechanisms and Catalysis*; Academic: New York, 1978.
(12) Marzilli, L. G.; Marzilli, P. A.; Halpern, J. *J. Am. Chem. Soc.* **1970**, *92*, 5752.
(13) (a) Hepp, A. F.; Wrighton, M. S. *J. Am. Chem. Soc.* **1981**, *103*, 1258. (b) Meyer, T. J.; Caspar, J. V. *Chem. Rev.* **1985**, *85*, 187.
(14) Nubel, P. O.; Brown, T. L. *J. Am. Chem. Soc.* **1982**, *104*, 4955.
(15) Hoffman, N. W.; Brown, T. L. *Inorg. Chem.* **1978**, *17*, 613.
(16) Darensbourg, D. J. *Adv. Organomet. Chem.* **1982**, *21*, 113.
(17) Hanckel, J. M.; Lee, K.-W.; Rushman, P. R.; Brown, T. L. *Inorg. Chem.* **1986**, *25*, 1852.
(18) Halpern, J. *Acc. Chem. Res.* **1970**, *3*, 386.
(19) Kidd, D. R.; Brown, T. L. *J. Am. Chem. Soc.* **1978**, *100*, 4095.
(20) Herberhold, M.; Razavi, A. *Angew. Chem., Int. Ed. Engl.* **1975**, *14*, 351.
(21) Howard, J. A.; Morton, J. R.; Preston, K. F. *Chem. Phys. Lett.* **1981**, *83*, 226.
(22) Symons, M. C. R.; Sweany, R. L. *Organometallics* **1982**, *1*, 834.
(23) (a) Tolman, C. A. *J. Am. Chem. Soc.* **1970**, *92*, 2953. (b) Tolman, C. A. *J. Am. Chem. Soc.* **1970**, *92*, 2956.
(24) Tolman, C. A. *Chem. Rev.* **1977**, *77*, 313.
(25) Cheng, A. H.; Shyong, P. J. *Proc. Natl. Sci. Counc., Repub. China, Part B* **1982**, *6*, 298.

0020-1669/89/1328-1059$01.50/0

which is crucial for obtaining optimal frozen-solution EPR spectra. The room-temperature EPR spectra were obtained by carefully thawing the samples for a short time (≅30 min). After collection of spectra, these samples were again quickly frozen in liquid nitrogen and checked to ensure that the thawing had produced no observable changes in their frozen-solution EPR spectra.

Liquid-nitrogen frozen-solution and room-temperature solution X-band (~9 GHz) EPR spectra were obtained with a Varian E-9 spectrometer with a standard TE_{102} microwave cavity system at the University of Illinois. For the liquid-nitrogen experiments, temperature was controlled by either a flow system or small quartz EPR immersion Dewar flask filled with liquid nitrogen. The usual precautions were taken to guard against spectral degradation caused by such common problems as water condensation in the cavity and microphonics from liquid-nitrogen bubbling. The frequency was measured with either a Hewlett-Packard frequency counter or calibration with finely powdered DPPH (α,α'-diphenyl-β-picrylhydrazyl). The magnetic field was measured with a Bruker tracking gaussmeter. Room-temperature frequencies are nominal.

Liquid-helium frozen-solution X-band (~9 GHz) and liquid-nitrogen frozen-solution S-band (~3 GHz) and L-band (~1.1 GHz) EPR spectra were obtained at the Medical College of Wisconsin with a standard Varian E-9 spectrometer and a Varian Century series EPR spectrometer fitted with a low-frequency microwave bridge and loop-gap resonator cavity system. For these experiments, the temperature was controlled with a flow system, the frequency measured with an EIP frequency counter, and the magnetic field monitored with a Radzipan tracking gaussmeter.

Simulations. The EPR simulations employed our program QPOWA, which has been previously described elsewhere[26-29] and consequently will be only briefly summarized here. This particular version of the program utilizes some features of earlier programs of Pilbrow,[30,31] White,[32] and Northern[33] but refashions the problem using various strategies to optimize accuracy, improve efficiency, and minimize restrictions. QPOWA accepts the line shape (Gaussian or Lorentzian), line width matrix, microwave frequency, nuclear g factor, and spin Hamiltonian matrices for electronic Zeeman, hyperfine coupling, and nuclear quadrupole interactions for up to two isotopes with specified abundances. The principal axes of $\tilde{\mathbf{g}}$, $\tilde{\mathbf{A}}$, and $\tilde{\mathbf{P}}$ matrices are related via specified sets of Euler angles. For each magnetic field orientation (θ_j, ϕ_j) on a coarse angular grid, the spin Hamiltonian, given in eq 1, is diagonalized for the terms involving the

$$\mathbf{H}_{spin} = \beta\vec{B}\cdot\tilde{\mathbf{g}}\cdot\vec{S} - g_n\beta_n\vec{B}\cdot\vec{I} + h(\vec{I}\cdot\tilde{\mathbf{A}}\cdot\vec{S} + \vec{I}\cdot\tilde{\mathbf{P}}\cdot\vec{I}) \quad (1)$$

central atom. Superhyperfine interactions with up to four additional nuclei are then added via perturbation theory. Transition fields (B_{kj}) are calculated from the energy eigenvalues by means of the first-order frequency-shift perturbation formula.[34] The peak transition intensities (J_{kj}) are calculated from the eigenvectors with allowances being made for all possible orientations of the oscillating magnetic field vector, spatial variation of the g factor in the oscillating field direction,[35] and integrated intensity variation with orientation associated with the transformation $J(\nu) \rightarrow J(B)$.[36] Transition fields (B_{kj}), peak transition intensities (J_{kj}), and line widths (W_{kj}) are then interpolated on other intermediate orientations to increase the sample density; each line is spread into a band; a two-dimensional Gaussian quadrature is carried out on the intensity for each field value, a weighted average over isotopes is computed, and the resulting spectrum is scaled and plotted. Parameters are adjusted, and the process is repeated until one is satisfied with the resemblance of the simulated spectrum to the experimental spectrum.

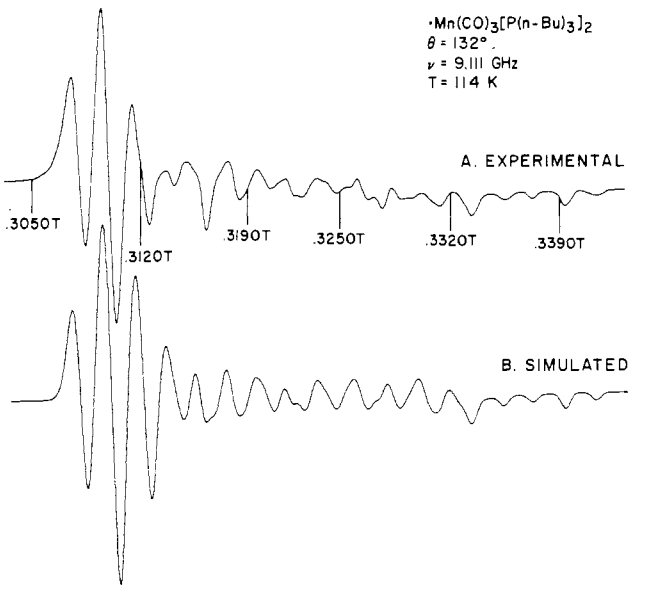

Figure 1. (A) Experimental liquid-nitrogen frozen-solution X-band ·$Mn(CO)_3[P(n\text{-}Bu)_3]_2$ EPR spectrum (1 tesla (T) = 10^4 G). (B) Computer-simulated spectrum.

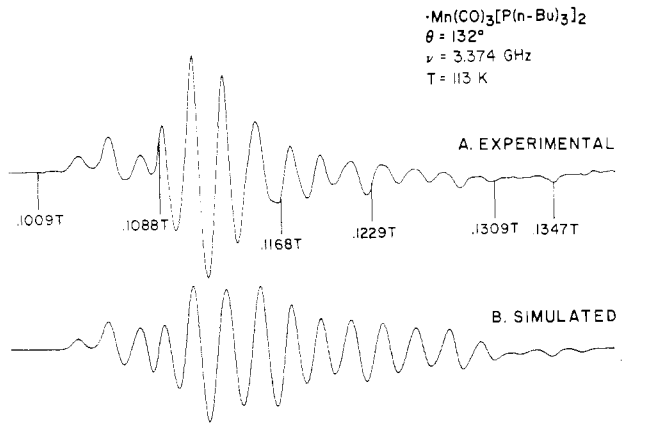

Figure 2. (A) Experimental liquid-nitrogen frozen-solution S-band ·$Mn(CO)_3[P(n\text{-}Bu)_3]_2$ EPR spectrum (1 tesla (T) = 10^4 G). (B) Computer-simulated spectrum.

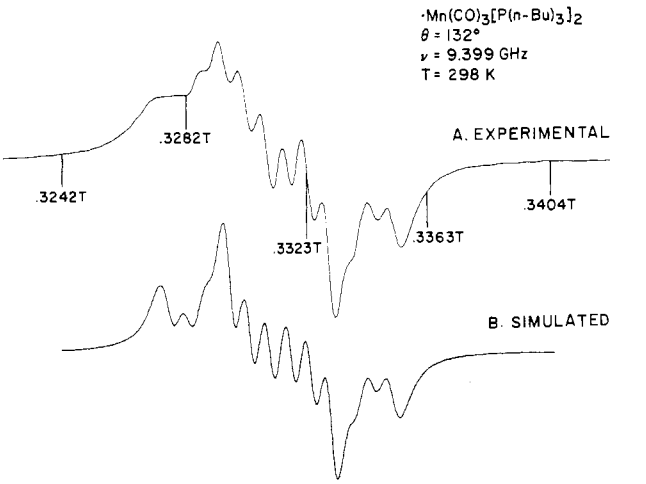

Figure 3. (A) Experimental room-temperature solution X-band ·$Mn(CO)_3[P(n\text{-}Bu)_3]_2$ EPR spectrum (1 tesla (T) = 10^4 G). (B) Computer-simulated spectrum.

For the ·$Mn(CO)_3L_2$ systems studied, the quadrupole and nuclear Zeeman interactions were omitted. Electronic Zeeman, metal atom hyperfine, and phosphorus superhyperfine interactions were included. The two phosphorus atoms were satisfactorily treated as equivalent. Axis systems of the $\tilde{\mathbf{g}}$, $\tilde{\mathbf{A}}_{Mn}$, and $\tilde{\mathbf{A}}_P'$ matrices were all assumed to be coincident

(26) Belford, R. L. Presented at the International ESR Symposium, Royal Dutch Chemical Society and The Chemical Society, Nijmegen, Holland, Aug 1977.
(27) Nilges, M. J. Ph.D. Dissertation, University of Illinois, Urbana, IL, 1978.
(28) Belford, R. L.; Nilges, M. J. Presented at the Symposium on EPR Spectroscopy, 21st Rocky Mountain Conference on Analytical Chemistry, Denver, CO, Aug 1979.
(29) Maurice, A. M. Ph.D. Dissertation, University of Illinois, Urbana, IL, 1982.
(30) Pilbrow, J. R.; Winfield, M. E. *Mol. Phys.* **1973**, *25*, 1073.
(31) Toy, A. D.; Chaston, S. H. H.; Pilbrow, J. R. *Inorg. Chem.* **1971**, *10*, 2219.
(32) White, L. K. Ph.D. Dissertation, University of Illinois, Urbana, IL, 1975.
(33) Northern, T. M. Ph.D. Dissertation, University of Illinois, Urbana, IL, 1976.
(34) Belford, R. L.; Davis, P. H.; Belford, G. G.; Lenhardt, T. M. *ACS Symp. Ser.* **1974**, *No. 40*, 5.
(35) Pilbrow, J. R. *Mol. Phys.* **1969**, *16*, 307.
(36) Aasa, R.; Vanngard, T. *J. Magn. Reson.* **1975**, *19*, 308.

Table I. EPR Parameters for $\cdot Mn(CO)_3[P(n\text{-}Bu)_3]_2$ in Hexane Solution

	X-band frozen	S-band frozen	X-band fluid
ν, GHz	9.111	3.374	9.399
$g_{\parallel}$	2.007 ± 0.002	2.005 ± 0.002	
$A_{\parallel Mn}$, MHz	(+)164 ± 8	(+)164 ± 8	
$A_{\parallel P}$, MHz	57 ± 3	57 ± 3	
$g_{\perp}$	2.036 ± 0.002	2.034 ± 0.002	
$A_{\perp Mn}$, MHz	(−)114 ± 6	(−)114 ± 6	
$A_{\perp P}$, MHz	58 ± 3	58 ± 3	
g_{iso}			2.026 ± 0.002
$A_{iso Mn}$, MHz			(−)19 ± 1
$A_{iso P}$, MHz			58 ± 3
line shape	Gaussian	Gaussian	Lorentzian
line width, MHz (half-width at half-height)	⊥ 20.00	⊥ 15.00	16.00
	∥ 9.65	∥ 12.30	
temp, K	114	113	298

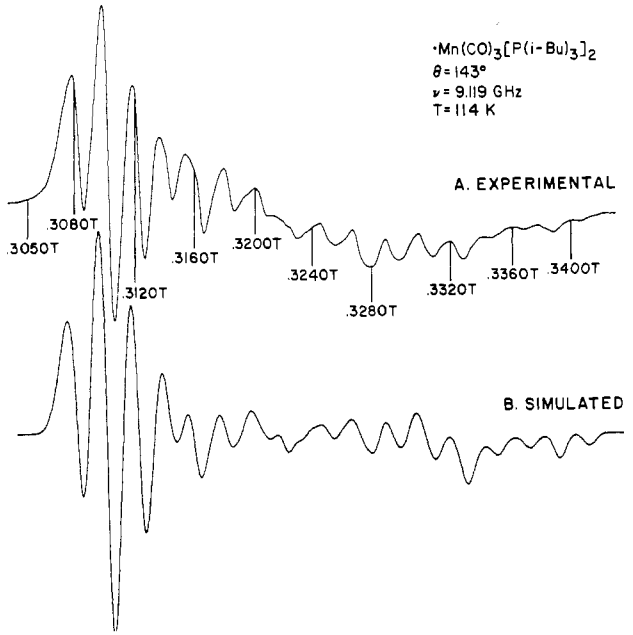

Figure 4. (A) Experimental liquid-nitrogen frozen-solution X-band $\cdot Mn(CO)_3[P(i\text{-}Bu)_3]_2$ EPR spectrum (1 tesla (T) = 10^4 G). (B) Computer-simulated spectrum.

in order to make the simulation problem more tractable. For a pseudoaxial system (^{55}Mn, $I = {}^5/_2$; two ^{31}P, $I = {}^1/_2$) at least 36 canonical features are expected in the frozen-solution EPR spectrum. Spin Hamiltonian parameters determined by *independent* simulation fits at each microwave frequency (X-band and S-band) for the frozen-solution spectra provided estimates of errors in the parameters by difference. On account of the restrictions imposed, the dubious assumption that the major paramagnetic species is unaccompanied by isomers or other contaminants and the self-imposed limitations on refinement cycles, simulations were never perfect. Therefore, in all cases attempts were made to fit both S- and X-band spectra equally well with nearly identical parameters. Choice of the line shape (restricted for tractability to either Gaussian or Lorentzian in the current program) was determined by comparing the observed line widths at half-height and quarter-height of the most clear-cut feature with the ideal Lorentzian and Gaussian values. (More realistically, the line shape should be close to a Voigt shape—a Gaussian convolution of Lorentzians.) EPR line shapes in glasses[37-39] and powders[38,40] have been discussed elsewhere.

Results

Figures 1–3 compare simulated and experimental frozen-solution X- and S-band and room-temperature solution X-band spectra of the $\cdot Mn(CO)_3[P(n\text{-}Bu)_3]_2$ radical. The EPR parameters obtained from the simulations are summarized in Table I.

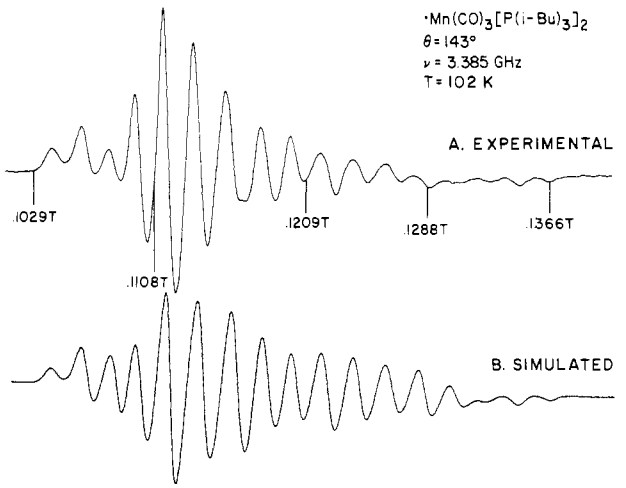

Figure 5. (A) Experimental liquid-nitrogen frozen-solution S-band $\cdot Mn(CO)_3[P(i\text{-}Bu)_3]_2$ EPR spectrum (1 tesla (T) = 10^4 G). (B) Computer-simulated spectrum.

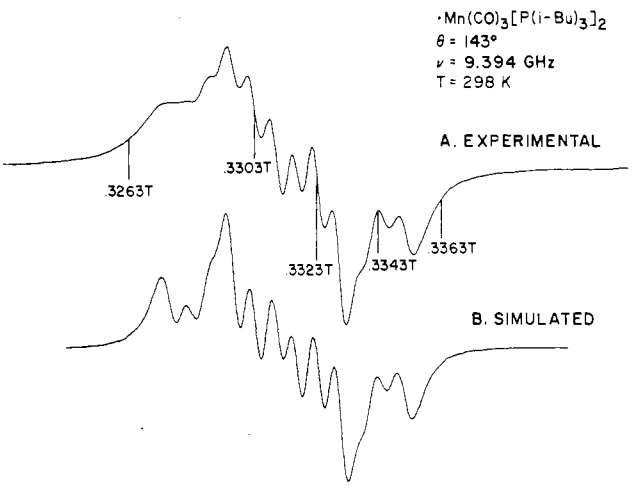

Figure 6. (A) Experimental room-temperature solution X-band $\cdot Mn(CO)_3[P(i\text{-}Bu)_3]_2$ EPR spectrum (1 tesla (T) = 10^4 G). (B) Computer-simulated spectrum.

Table II. EPR Parameters for $\cdot Mn(CO)_3[P(i\text{-}Bu)_3]_2$ in Hexane Solution

	X-band frozen	S-band frozen	X-band fluid
ν, GHz	9.119	3.385	9.394
$g_{\parallel}$	2.006 ± 0.008	2.013 ± 0.008	
$A_{\parallel Mn}$, MHz	(+)165 ± 8	(+)162 ± 8	
$A_{\parallel P}$, MHz	54 ± 3	57 ± 3	
$g_{\perp}$	2.035 ± 0.008	2.043 ± 0.008	
$A_{\perp Mn}$, MHz	(−)116 ± 6	(−)114 ± 6	
$A_{\perp P}$, MHz	58 ± 3	58 ± 3	
g_{iso}			2.025 ± 0.008
$A_{iso Mn}$, MHz			(−)20 ± 1
$A_{iso P}$, MHz			57 ± 3
line shape	Gaussian	Gaussian	Lorentzian
line width, MHz (half-width at half-height)	⊥25.00	⊥16.00	16.00
	∥12.98	∥13.14	
temp, K	114	102	298

Simulated and experimental EPR spectra are compared for the $\cdot Mn(CO)_3[P(i\text{-}Bu)_3]_2$ system in Figures 4–6; the EPR parameters are summarized in Table II. The frozen solutions of both the $P(n\text{-}Bu)_3$ and $P(i\text{-}Bu)_3$ systems were successfully simulated under an axial assumption. For an $S = {}^1/_2$ system with an $I = {}^5/_2$ principal nucleus and two equivalent and resolvable superhyperfine nuclei with nuclear spins $I = {}^1/_2$, a minimum of 36 allowed ($\Delta M_S = \pm 1$, $\Delta M_I = 0$) transitions (on-axis extrema) are expected in the frozen-solution spectra if only one paramagnetic species is present. It is noteworthy that despite an R_3P cone angle difference

(37) Sands, R. H. *Phys. Rev.* **1955**, *99*, 1222.
(38) Kneubühl, F. K. *J. Chem. Phys.* **1960**, *33*, 1074.
(39) Neiman, R.; Kivelson, D. *J. Chem. Phys.* **1961**, *35*, 156.
(40) Weil, J. A.; Hecht, H. G. *J. Chem. Phys.* **1963**, *38*, 281.

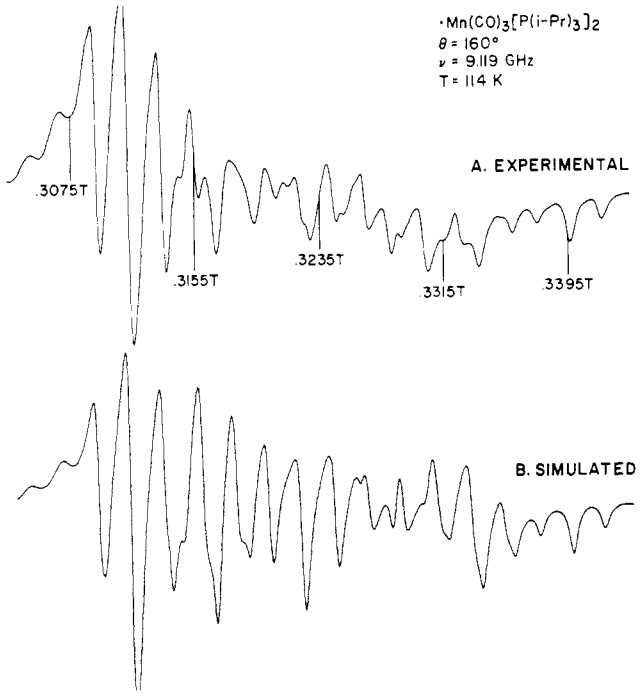

Figure 7. (A) Experimental liquid-nitrogen frozen-solution X-band $\cdot Mn(CO)_3[P(i\text{-}Pr)_3]_2$ EPR spectrum (1 tesla (T) = 10^4 G). (B) Computer-simulated spectrum.

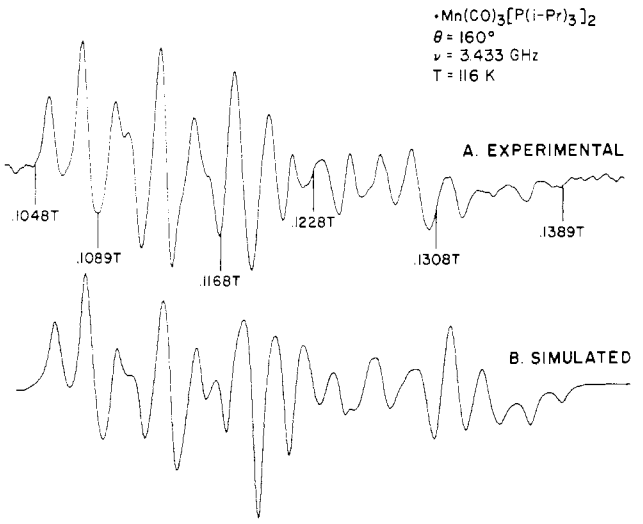

Figure 8. (A) Experimental liquid-nitrogen frozen-solution S-band $\cdot Mn(CO)_3[P(i\text{-}Pr)_3]_2$ EPR spectrum (1 tesla (T) = 10^4 G). (B) Computer-simulated spectrum.

of 11°[24] the EPR spectra of the $P(n\text{-}Bu)_3$ and $P(i\text{-}Bu)_3$ radicals are essentially identical (see Discussion). In the X-band frozen-solution EPR spectra, the low-field edges are composed of superimposed parallel and perpendicular phosphorus triplets while the middle regions and high-field edges are composed of overlapping parallel and perpendicular spectral features and parallel phosphorus triplets, respectively.

In the S-band frozen-solution EPR spectra, the low-field parallel phosphorus triplets have been separated from the low-field perpendicular features, thus facilitating analysis. The need for multifrequency EPR spectroscopy will be discussed in the next section. The simulated and experimental EPR spectra of the $\cdot Mn(CO)_3[P(i\text{-}Pr)_3]_2$ radical are compared in Figures 7–9. An axial fit was insufficient; consequently, rhombic terms were added. The EPR parameters obtained are summarized in Table III. Figures 10–12 compare simulated EPR spectra with experimental EPR spectra of the phosphite radical $\cdot Mn(CO)_3[P(O\text{-}i\text{-}Pr)_3]_2$. In the frozen-solution X-band EPR spectrum the low-field spectral edge is composed of two overlapping perpendicular phosphorus

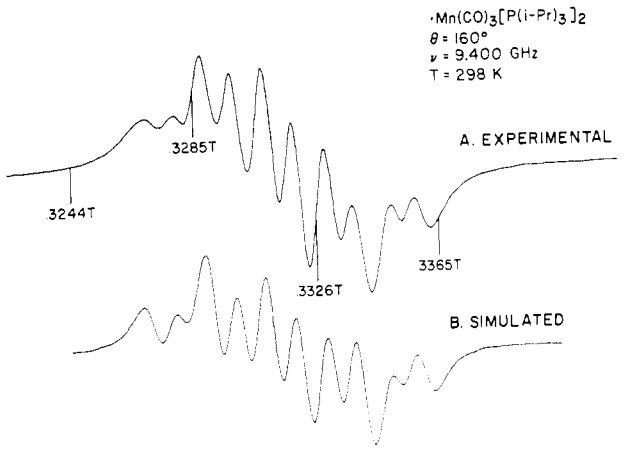

Figure 9. (A) Experimental room-temperature solution X-band $\cdot Mn(CO)_3[P(i\text{-}Pr)_3]_2$ EPR spectrum (1 tesla (T) = 10^4 G). (B) Computer-simulated spectrum.

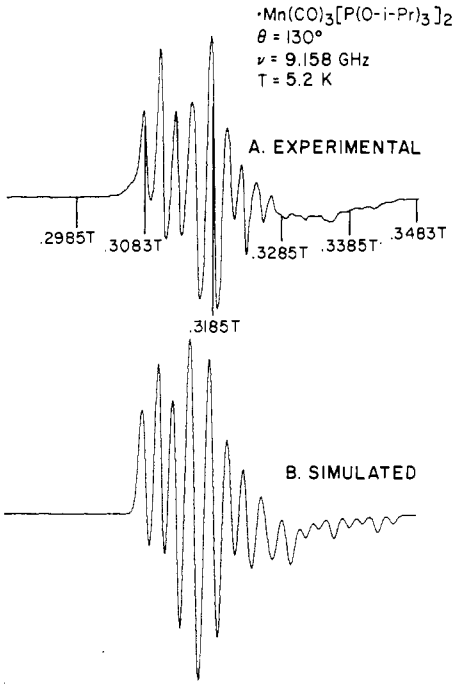

Figure 10. (A) Experimental liquid-helium frozen-solution X-band $\cdot Mn(CO)_3[P(O\text{-}i\text{-}Pr)_3]_2$ EPR spectrum (1 tesla (T) = 10^4 G). (B) Computer-simulated spectrum.

Table III. EPR Parameters for $\cdot Mn(CO)_3[P(i\text{-}Pr)_3]_2$ in Hexane Solution

	X-band frozen	S-band frozen	X-band fluid
ν, GHz	9.119	3.433	9.400
g_x	2.047 ± 0.002	2.049 ± 0.002	
$A_{x_{Mn}}$, MHz	(−)135 ± 7	(−)135 ± 7	
A_{x_P}, MHz	57 ± 3	58 ± 3	
g_y	2.023 ± 0.002	2.025 ± 0.002	
$A_{y_{Mn}}$, MHz	(−)120 ± 6	(−)120 ± 6	
A_{y_P}, MHz	58 ± 3	57 ± 3	
g_z	2.004 ± 0.008	2.012 ± 0.008	
$A_{z_{Mn}}$, MHz	(+)158 ± 8	(+)165 ± 8	
A_{z_P}, MHz	58 ± 3	57 ± 3	
g_{iso}			2.025 ± 0.004
$A_{iso_{Mn}}$, MHz			(−)27 ± 1
A_{iso_P}, MHz			58 ± 3
line shape	Lorentzian	Lorentzian	Lorentzian
line width, MHz	x 22.0	x 19.32	18.00
(half-width at	y 10.00	y 19.32	
half-height)	z 9.10	z 12.70	
temp, K	114	116	298

triplets and overlapping parallel phosphorus triplets that at first glance resemble two separate phosphorus triplets. The EPR

Table IV. EPR Parameters for $\cdot Mn(CO)_3[P(O\text{-}i\text{-}Pr)_3]_2$ in Hexane Solution

	X-band frozen	S-band frozen	X-band fluid
ν, GHz	9.158	3.357	9.399
$g_\parallel$	1.999 ± 0.008	1.99 ± 0.008	
$A_{\parallel_{Mn}}$, MHz	(+)176 ± 9	(+)176 ± 9	
$A_{\parallel_P}$, MHz	63 ± 3	63 ± 3	
$g_\perp$	2.044 ± 0.008	2.004 ± 0.008	
$A_{\perp_{Mn}}$, MHz	(−)71 ± 4	(−)71 ± 4	
$A_{\perp_P}$, MHz	78 ± 4	78 ± 4	
g_{iso}			2.029 ± 0.008
$A_{iso_{Mn}}$, MHz			(+)11.6 ± 0.6
A_{iso_P}, MHz			70 ± 4
line shape	Gaussian	Gaussian	Lorentzian
line width, MHz (half-width at half-height)	⊥ 26.57	⊥ 23.70	30.00
	∥ 15.74	∥ 19.00	
temp, K	5.2	135	

parameters are summarized in Table IV.

It is noteworthy that in the phosphite system the phosphorus interaction shows marked anisotropy and that the perpendicular manganese hyperfine interaction is dramatically smaller than the corresponding interaction in the phosphine systems. Comments are in order regarding the most troublesome simulation, that of the S-band frozen-solution spectrum shown in Figure 11. While this simulation has the general appearance of the experimental spectrum, the center portion, i.e., the part that includes the perpendicular lines, does not quite match. In particular, the phase of the oscillations is shifted. The g_x, g_y, A_x, and A_y values were carefully varied over a considerable range, and **g** and $\mathbf{A}_{Mn}$ tensor axes were set noncoincident over a considerable range (up to 45° between their z axes) to no avail. Many aspects of this particular system may contribute to the simulation difficulty. In order to simplify the simulation of these complicated systems, several assumptions were made: (1) $\tilde{\mathbf{A}}_{Mn}$ and $\tilde{\mathbf{A}}_P'$ tensor axis coincidence; (2) phosphorus atom equivalence; (3) no line width or line shape variation with orientation or M_I line number; (4) the presence of only one paramagnetic manganese species. Since there is phosphorus anisotropy in this system, restrictions 1 and 2 may be particularly severe. The magnetic field measurements were less accurate in this case than in the others. Because of these difficulties, the computer-simulated spectrum shown in Figure 11 is that with the same axial spin Hamiltonian parameters employed for the liquid-helium X-band simulation shown in Figure 10. We judge that any improvements to be obtained from a great deal of additional effort, either in the computations or in the experiments (including a repeat of the synthesis and spectroscopy), would be merely cosmetic and could produce little change in the derived parameters.

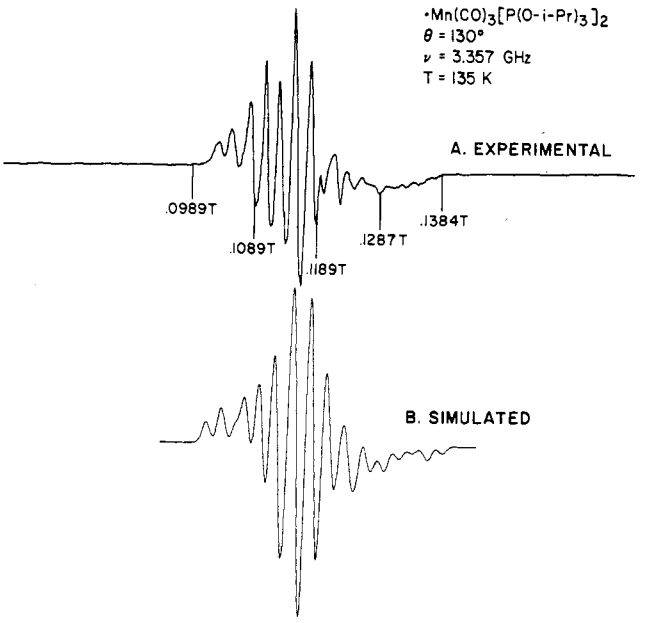

Figure 11. (A) Experimental liquid-nitrogen frozen-solution S-band $\cdot Mn(CO)_3[P(O\text{-}i\text{-}Pr)_3]_2$ EPR spectrum (1 tesla (T) = 10^4 G). (B) Computer-simulated spectrum (field scale expanded by 3.5% and shifted several gauss as noted in text).

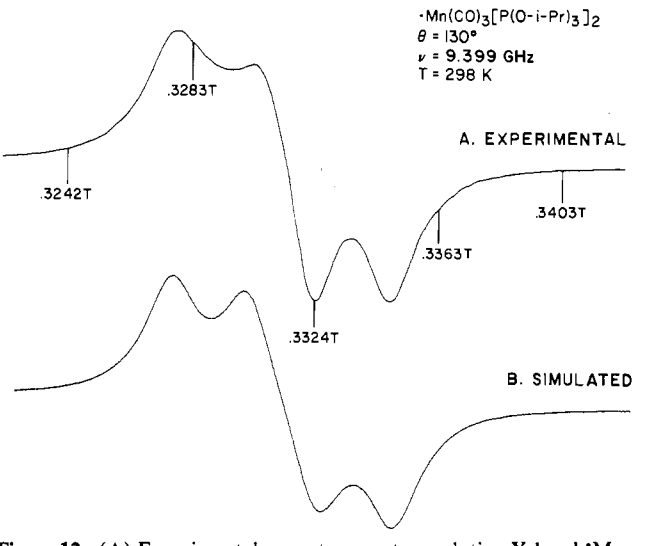

Figure 12. (A) Experimental room-temperature solution X-band $\cdot Mn(CO)_3[P(O\text{-}i\text{-}Pr)_3]_2$ EPR spectrum (1 tesla (T) = 10^4 G). (B) Computer-simulated spectrum.

Discussion

Qualitative Aspects. The averages of the parameters for the frozen-solution X-band and S-band EPR spectra of the four systems studied are summarized in Table V. The parallel g values (g_z) for all of the $\cdot Mn(CO)_3L_2$ systems are close to the free-electron value (g_e = 2.0023). All of the (tertiary phosphine)-manganese systems have very similar parallel manganese hyperfine interactions ($A_{z_{Mn}}$), while in the phosphite system the $A_{z_{Mn}}$ is somewhat larger. The phosphorus superhyperfine interaction is

Table V. Average EPR Parameters for Frozen-Solution X- and S-Band EPR Spectra of $\cdot Mn(CO)_3L_2$ Species in Hexane

	L			
	$P(n\text{-}Bu)_3$	$P(i\text{-}Bu)_3$	$P(i\text{-}Pr)_3$	$P(O\text{-}i\text{-}Pr)_3$[a]
θ, deg	132	143	160	130[32]
ν_{CO}, cm^{-1}	2060.3[32]	2059.7[32]	2059.2[32]	2075.9[32]
g_z	2.006 ± 0.001	2.010 ± 0.004	2.008 ± 0.004	1.999 ± 0.008
$A_{z_{Mn}}$, MHz	(+)164 ± 8	(+)164 ± 8	(+)162 ± 8	(+)176 ± 9
A_{z_P}, MHz	57 ± 3	56 ± 3	58 ± 3	63 ± 3
g_x	2.035 ± 0.001	2.039 ± 0.004	2.048 ± 0.001	2.044 ± 0.008
$A_{x_{Mn}}$, MHz	(−)114 ± 6	(−)115 ± 6	(−)135 ± 7	(−)71 ± 4
A_{x_P}, MHz	58 ± 6	58 ± 3	58 ± 3	78 ± 4
g_y	2.035 ± 0.001	2.039 ± 0.004	2.024 ± 0.001	2.044 ± 0.008
$A_{y_{Mn}}$, MHz	(−)114 ± 6	(−)115 ± 6	(−)120 ± 6	(−)71 ± 4
A_{y_P}, MHz	58 ± 3	58 ± 3	58 ± 3	78 ± 4
line shape	Gaussian	Gaussian	Lorentzian	Gaussian

[a] X-Band parameters only.

Table VI. Calculated K_b^2 Values for $^{\bullet}Mn(CO)_3L_2$ Systems

$^{\bullet}Mn(CO)_3L_2$	Δg $(g_\perp - g_e)$	ΔA $(A_{\perp_{Mn}} - A_{\parallel_{Mn}})$, MHz	K_b^2
$^{\bullet}Mn(CO)_3[P(n\text{-}Bu)_3]_2$	0.0327	−278	0.60 ± 0.03
$^{\bullet}Mn(CO)_3[P(i\text{-}Bu)_3]_2$	0.0367	−279	0.61 ± 0.03
$^{\bullet}Mn(CO)_3[P(i\text{-}Pr)_3]_2$	0.0337	−289	0.62 ± 0.03
$^{\bullet}Mn(CO)_3[P(O\text{-}i\text{-}Pr)_3]_2$	0.0417	−247	0.56 ± 0.03
$^{\bullet}Mn(CO)_5$[a]	0.0357	−288	0.62 ± 0.03

[a] Values from ref 21 and 41.

essentially isotropic and is of the same magnitude in all three manganese tertiary phosphine systems. In the phosphite system, however, the phosphorus superhyperfine interaction not only is larger than that of the phosphorus system but also has noticeable anisotropy. Presumably, this results from more extensive back-bonding into the π-system of the phosphorus atom in the phosphite ligand. The $^{\bullet}Mn(CO)_3[P(i\text{-}Pr)_3]_2$ radical system is unique in having considerable rhombic character as well as a predominantly Lorentzian line shape. The perpendicular g values (g_x and g_y) are all substantially shifted from the free-electron value. In the $^{\bullet}Mn(CO)_3[P(n\text{-}Bu)_3]_2$ and $^{\bullet}Mn(CO)_3[P(i\text{-}Bu)_3]_2$ systems the perpendicular g values as well as the perpendicular hyperfine values are practically identical. In other words, the environments in which the unpaired spin resides are very similar in these two systems despite a cone angle difference of 11°.[24] The average of g_x and g_y for $^{\bullet}Mn(CO)_3[P(i\text{-}Pr)_3]_2$, 2.036, is close to $g_\perp$ for both $^{\bullet}Mn(CO)_3[P(n\text{-}Bu)_3]_2$ and $^{\bullet}Mn(CO)_3[P(i\text{-}Bu)_3]_2$. The average of $A_{x_{Mn}}$ and $A_{y_{Mn}}$, 128 MHz, however, is somewhat larger than the corresponding perpendicular hyperfine interaction in the $^{\bullet}Mn(CO)_3[P(n\text{-}Bu)_3]_2$ and $^{\bullet}Mn(CO)_3[P(i\text{-}Bu)_3]_2$ radicals. The $^{\bullet}Mn(CO)_3[P(i\text{-}Pr)_3]_2$ system, while somewhat different, appears to be more like the other pseudoaxial tertiary phosphine $^{\bullet}Mn(CO)_3L_2$ (L = $P(n\text{-}Bu)_3$, $P(i\text{-}Bu)_3$) systems than one might suspect from a casual observation of their rather different-looking spectra, despite the large variation in the cone angle parameter ($\Delta\theta$ = 28°[24]). In contrast, the phosphite system, $^{\bullet}Mn(CO)_3[P(O\text{-}i\text{-}Pr)_3]_2$, is markedly different from the tertiary phosphine systems. The perpendicular g value is shifted a bit further from the free-electron value, and the perpendicular hyperfine interaction is dramatically smaller than the corresponding interaction in the tertiary phosphine systems. The phosphite ligand has approximately the same steric requirement as the $P(n\text{-}Bu)_3$ ligand but is electronically markedly different.[24] Presumably, the difference in π-acidity between tertiary phosphines and phosphites affects the environment in which the unpaired spin resides.

Theoretical Aspects. The resulting g shifts and hyperfine shifts for d^7 $^{\bullet}Mn(CO)_3L_2$ radical systems in an axial square-pyramidal (C_{4v}) field were derived in detail.[41] The perturbation Hamiltonian employed with terms listed in order of decreasing magnitude is given in eq 2, where λ = spin–orbit coupling constant, $\vec{l}_k$ = orbital

$$H'_{pert} = \underbrace{\sum_{k=1}^{3} \lambda \vec{l}_k \cdot \vec{s}_k}_{\text{SO coupling}} + \underbrace{\sum_{k=1}^{3} \beta(\vec{l}_k + g_e\vec{s}_k)\cdot\vec{B}}_{\text{Zeeman interacn}} + \underbrace{2g_n\beta\beta_n\langle r_{nd}^{-3}\rangle \sum_{k=1}^{3} \vec{l}\cdot\vec{I}_k}_{\text{nuclear spin-electron orbit interacn}} + \underbrace{-g_e g_n \beta\beta_n \langle r_{nd}^{-3}\rangle \sum_{k=1}^{3} (\vec{s}_k\cdot\vec{I} - 3(\vec{s}_k\cdot\vec{r}_k)(\vec{I}\cdot\vec{r}_k))}_{\text{anisotropic hyperfine interacn}} \quad (2)$$

angular momentum operator for electron k, $\vec{s}_k$ = spin angular momentum operator for electron k, β and β_n = Bohr and nuclear magnetons, respectively, g_e and g_n are free-electron spin and metal nucleus g factors, respectively, $\vec{B}$ = external magnetic induction, $\langle r_{nd}^{-3}\rangle$ = average value of inverse cubed radius of any nd electron, $\vec{I}$ = spin angular momentum operator of the metal nucleus, and $\vec{r}_k$ = direction cosine vector of the kth electron from the metal nucleus. For this axial approximation, the hole formalism was utilized. A basis set of 22 wave functions using Slater determinantal spin orbitals of the metal d orbitals was constructed for the axial C_{4v} symmetry system as an approximation to the C_{2v} symmetry orthorhombic case. Spin–orbit coupling, Zeeman effect, anisotropic hyperfine, and orbital perturbations were applied to the system. In addition a zero-differential-overlap approximation was used in which only one-center metal orbital–metal orbital overlap terms survived. The calculated results for the Zeeman and anisotropic hyperfine interactions are given in eq 3–6, where

$$g_\parallel = g_e \quad (3)$$

$$A_\parallel = \frac{-4K_b^2 T}{7} \quad (4)$$

$$g_\perp = g_e + \frac{6\lambda K_b^2 K_d^2}{\Delta E} \quad (5)$$

$$A_\perp = \frac{2K_b^2 T}{7} + \frac{12K_b^2 K_d^2 R\lambda}{\Delta E} \quad (6)$$

K_b = molecular orbital coefficient for the $3d_{z^2}$ orbital in the SOMO, K_d = molecular orbital coefficient for the $3d\pi$ orbitals (d_{xz} and d_{yz}) in excited-state SOMO's, ΔE = energy difference between the ground state and excited state, $R = 2g_n\beta\beta_n\langle r_{3d}^{-3}\rangle$, and $T = -2.0023g_n\beta\beta_n\langle r_{3d}^{-3}\rangle$. It is interesting to note in eq 6 the term $12K_b^2K_d^2R\lambda/\Delta E$, contributed by the nuclear spin–electron orbit interaction, which is often omitted from the perturbation Hamiltonian. The noncontact hyperfine interaction is thus not predicted to average to zero and will contribute to the observed isotropic hyperfine splitting.

Unpaired Spin Density Localized on the Mn $3d_{z^2}$ Orbital. The above expressions for the g factors and A values can be used along with the experimentally obtained values to calculate K_b^2, the unpaired spin density in the $3d_{z^2}$ orbital. The parameters obtained experimentally are given in Table V. The shift from the free-electron g value is given in eq 7. The difference between the

$$\Delta g = \frac{6\lambda K_b^2 K_d^2}{\Delta E} \quad (7)$$

calculated $A_\perp$ and $A_\parallel$ expressions can be used with the experimentally obtained hyperfine parameters.

$$\Delta A = A_\perp - A_\parallel = \frac{6K_b^2 T}{7} + \frac{12K_b^2 K_d^2 R\lambda}{\Delta E} \quad (8)$$

Elimination of the quantity $\lambda K_b^2 K_d^2$ in eq 7 and 8 yields the expression

$$K_b^2 = \frac{7}{6T}(-2R\Delta g + \Delta A) \quad (9)$$

The values of T ($T = -2.0023g_n\beta\beta_n\langle r_{3d}^{-3}\rangle$) and R ($R = 2g_n\beta\beta_n\langle r_{3d}^{-3}\rangle$) were calculated from atomic parameters computed by Morton and Preston[42] and the nuclear g values for manganese. We obtained values of T_{Mn} and R_{Mn} equal to −622 and 621 MHz, respectively, by using, for ^{55}Mn in a 4s3d configuration, $\langle r_{3d}^{-3}\rangle$ = 4.721 au.

Now one can calculate the unpaired spin density in the d_{z^2} orbital (K_b^2) by using eq 9 and determining the signs of the metal hyperfine coupling constants. By analogy to a previous assignment[21] for the $^{\bullet}Mn(CO)_5$ coupling constants ($A_{\perp_{Mn}}/g\beta = -30 \pm 3$ G; $A_{\parallel_{Mn}}/g\beta = 66 \pm 3$ G) and the results from the theoretical calculation,[41] the perpendicular metal hyperfine coupling constant is assigned a negative value and the parallel metal hyperfine coupling constant is assigned a positive value. The g factors and A values reported in Table V are used. For the $^{\bullet}Mn(CO)_3[P(i\text{-}Pr)_3]_2$ calculation, the average values of g_x and g_y and of $A_{x_{Mn}}$ and $A_{y_{Mn}}$ are used for $g_\perp$ and $A_\perp$, respectively. The results obtained are summarized in Table VI. For the manganese tertiary phosphine systems, the unpaired spin density in the manganese $3d_{z^2}$ orbital is essentially identical for all three systems (≈60%). The unpaired spin density in the manganese $3d_{z^2}$ orbital in the

(41) Rattinger, G. B. Ph.D. Dissertation, University of Illinois, Urbana, IL, 1984.

(42) Morton, J. R.; Preston, K. F. *J. Magn. Reson.* **1978**, *30*, 577.

Table VII. Lower Limit ($\chi_0 = -1.0$ au) and Upper Limit ($\chi_0 = -3.0$ au) Values for Isotropic Hyperfine Terms for $\cdot Mn(CO)_3L_2$ Systems

	$\cdot Mn(CO)_3[P(n\text{-}Bu)_3]_2$	$\cdot Mn(CO)_3[P(i\text{-}Bu)_3]_2$	$\cdot Mn(CO)_3[P(i\text{-}Pr)_3]_2$	$\cdot Mn(CO)_3[P(O\text{-}i\text{-}Pr)_3]_2$
g_{iso}	2.026 ± 0.002	2.025 ± 0.008	2.025 ± 0.004	2.029 ± 0.008
$A_{iso_{Mn}}$, MHz	(−)19 ± 1	(−)20 ± 1	(−)27 ± 1	(+)12 ± 1
A_{iso_P}, MHz	58 ± 3	57 ± 3	58 ± 3	70 ± 4
K_b^2	0.60	0.61	0.62	0.56
$A^\circ_{iso_{Mn},SP}$, MHz	−89 → −263	−89 → −263	−89 → −263	−89 → −263
$K_b^2 A^\circ_{iso_{Mn},SP}$, MHz	−53 → −158	−54 → −160	−55 → −163	−50 → −147
$A_{iso_{Mn},\vec{l}\cdot\vec{L}}$, MHz	27	30	28	35
$A_{iso_{Mn},direct}$, MHz	7.3 → 112	4.0 → 110	0.0 → 108	27 → 124

phosphite system is 56%, slightly lower than in the tertiary phosphine systems; however, the difference is barely outside our estimated error limits. Presumably, the lower value for the phosphite system is a consequence of the better π-acid capabilities of the phosphite ligand. Since the steric requirements of $P(O\text{-}i\text{-}Pr)_3$ and $P(n\text{-}Bu)_3$ are essentially identical (for $P(O\text{-}i\text{-}Pr)_3$, $\theta = 130°$; for $P(n\text{-}Bu)_3$, $\theta = 132°$[24]), it seems reasonable that the phosphite is better able than the tertiary phosphines to compete with the carbonyl ligands for electron density from the manganese center. This is supported by the carbonyl infrared stretching data[9] and the electronic parameters.[24]

Howard, Morton, and Preston[21] have reported 51% unpaired spin density in the $3d_{z^2}$ orbital for the $\cdot Mn(CO)_5$ system, but their calculation did not include the nuclear spin–orbit coupling interaction. For $\cdot Mn(CO)_5$, using their values ($g_\perp = 2.038 \pm 0.003$; $g_\parallel = 2.000 \pm 0.003$; $A_\perp = -30 \pm 3$ G ≈ -90 MHz; $A_{\parallel_{Mn}} = 66 \pm 3$ G ≈ 198 MHz) and eq 9, we obtain a K_b^2 value of 0.62 as reported in Table VI. Thus, the unpaired spin density in the manganese $3d_{z^2}$ orbital calculated for the $\cdot Mn(CO)_5$ system with the inclusion of the nuclear spin–orbit coupling term is essentially identical with the corresponding densities for the disubstituted $\cdot Mn(CO)_3L_2$ tertiary phosphine systems. There may be more unpaired spin density in the carbonyl ligand π^* orbitals of the substituted radicals than in those of $\cdot Mn(CO)_5$. Because of solvent effects and other experimental variations, direct quantitative comparison with infrared data is difficult. For $\cdot Mn(CO)_5$, Turner and co-workers[43] have observed two carbonyl infrared stretching bands that they assigned to $\cdot Mn(CO)_5$: 1988 cm^{-1} (e mode (equatorial)) and 1978 cm^{-1} (a_1 mode (apical)). The infrared bands for all of the $\cdot Mn(CO)_3L_2$ systems[9] are shifted to lower frequency values from $\cdot Mn(CO)_5$. This shift may be indicative of increased electron density in the carbonyl ligand π^* orbitals. However, the experimental conditions are different and conclusions based on direct comparison of the infrared data must be regarded as tentative.

The g factors for the $\cdot Mn(CO)_3L_2$ systems reported in Table V are all very close to those of $\cdot Mn(CO)_5$.[21] The radical $\cdot Mn(CO)_3[P(O\text{-}i\text{-}Pr)_3]_2$ shows the largest deviation. Presumably, its excited state and ground state are closer together than in $\cdot Mn(CO)_5$ or the tertiary phosphine $\cdot Mn(CO)_3L_2$ systems. Consequently, larger g shifts are observed for the phosphite system. Electron density is most likely π-back-bonded into the empty phosphorus d orbitals in this system. However, in general, substitution of carbonyl ligands by phosphine or phosphite ligands does *not* greatly affect the amount of unpaired spin density in the ground-state $3d_{z^2}$ orbital. Since all of these 17e $\cdot Mn(CO)_3L_2$ radicals are metal-centered, it is not surprising that they have been found to undergo atom-transfer reactions.[9,44]

Energy Difference between Excited State and Ground State. The energy difference, ΔE, between the ground state and the $d\pi$ excited state for each $\cdot Mn(CO)_3L_2$ system can be estimated from the calculated K_b^2 value, Δg value, an estimate of the spin–orbit coupling constant (λ), and a range of K_d^2 values. The relationship given in eq 7 can be solved for ΔE. Figgis'[45] value of λ for Mn(0), −190 cm^{-1}, can be used. K_d^2 represents the approximate fractional metal $d\pi$ (d_{xz} and d_{yz}) content of an occupied $d\pi$ metal antibonding orbital in a perturbing excited-state component of the Kramers doublet. Therefore, a reasonable range of K_d^2 values is from 0.50 to 1.0.

Isotropic Interaction. The isotropic hyperfine parameters for the four $\cdot Mn(CO)_3L_2$ systems are summarized in Tables I–IV. These parameters were obtained by averaging the X-band frozen-solution parameters (see Tables I–IV). Consequently, the sign of the isotropic manganese hyperfine coupling constant is negative for all of the tertiary phosphine systems and positive for the phosphite systems. In addition, all of the isotropic g values, g_{iso}, are very similar. The isotropic manganese coupling constant in the $\cdot Mn(CO)_3[P(i\text{-}Pr)_3]_2$ systems is the most negative, presumably on account of a larger spin-polarization contribution (vide infra). The corresponding interaction in the phosphite system is positive, which is indicative of a smaller spin-polarization contribution in this system. In these $\cdot Mn(CO)_3L_2$ radical systems, there are three major sources that contribute to the isotropic metal hyperfine interaction. The direct mechanism is caused by direct hybridization of s character into the d_{z^2} orbital. In both C_{2v} and C_{4v} point groups s and d_{z^2} orbitals have A_1 symmetry. This direct mechanism is thus a Fermi contact that gives a positive contribution to the isotropic metal hyperfine coupling constant. It will be denoted $A_{iso_{Mn},direct}$. A second Fermi contact term arises from spin or core polarization of occupied s orbitals (mainly inner s orbitals). It is negative in sign and will be designated $K_b^2 A_{iso_{Mn},SP}$. It depends directly on the spin density in the $3d_{z^2}$ manganese orbital. The third major source of the isotropic metal hyperfine interaction is a noncontact term arising from nuclear spin–orbit coupling, $12K_b^2K_d^2R\lambda/\Delta E$. This term is induced by both the electron spin–orbit interaction and the electron spin–nuclear spin interaction. The isotropic part is two-thirds of the interaction and is positive in sign since both ΔE and λ are negative. This term will be designated $A_{iso_{Mn},\vec{l}\cdot\vec{L}}$ and is equal to $8K_b^2K_d^2R\lambda/\Delta E$.

Both the spin-polarization and nuclear spin–orbit coupling terms arise from configuration mixing. Consequently, when the overall sum of the interactions is small, a change in the sign of the isotropic coupling constant can be observed in a series of fairly similar radical species. The overall isotropic manganese hyperfine coupling constant can be expressed as a sum of these three terms.

Of all the radicals studied here, $\cdot Mn(CO)_3[P(i\text{-}Pr)_3]_2$ has the most negative isotropic manganese hyperfine coupling constant ($A_{iso_{Mn}} = -27$ MHz). Only the spin-polarization term, $K_b^2 A^\circ_{iso_{Mn},SP}$, makes a negative contribution to the isotropic interaction. Consequently, a scale relative to $\cdot Mn(CO)_3[P(i\text{-}Pr)_3]_2$ can be developed by assuming that $A_{iso_{Mn},direct}$ is zero in this system: lower limit values of the isotropic terms and the spin-polarization values, χ_0, can be calculated through McGarvey's equation for χ_0[46]. A lower limit of $\chi_0 = -1.0$ au is obtained. From a study of oxide lattice systems in the first transition series, McGarvey[46] has obtained a χ_0 value of −3.0 au for d^7 systems. Using $\chi_0 = 3.0$ au to calculate the spin-polarization term, $A^\circ_{iso_{Mn},SP}{}'$, one can obtain an upper limit on the $A_{iso_{Mn},direct}$ values for the $\cdot Mn(CO)_3L_2$ systems. Lower and upper limit isotropic interactions are summarized in Table VII.

Unpaired Spin Density Delocalized on the Manganese 4s Orbital and Phosphorus Ligands. An upper limit of the unpaired spin

(43) Church, S. P.; Poliakoff, M.; Timney, J. A.; Turner, J. J. *J. Am. Chem. Soc.* **1981**, *103*, 7515. The frequencies listed are for the all-^{12}CO species.
(44) Herrick, R. S.; Herrinton, T. R.; Walker, H. W.; Brown, T. L. *Organometallics* **1985**, *4*, 42.
(45) Figgis, B. N. *Introduction to Ligand Fields*; Wiley Interscience: New York, 1966; p 60.
(46) McGarvey, B. R. *J. Phys. Chem.* **1967**, *71*, 51.

Table VIII. Upper Limits of Unpaired Spin Density in the Manganese 4s Orbital and Phosphorus $3sp^3$ Hybrid Orbitals for $^{\bullet}Mn(CO)_3L_2$ Systems in Hexane

$^{\bullet}Mn(CO)_3L_2$	upper limit: $A_{iso_{Mn,direct}}$, MHz	upper limit: % Mn 4s character	A_{iso_P}, MHz	% $3sp^3$ phosphorus character (per PR ligand)
$^{\bullet}Mn(CO)_3[P(n\text{-}Bu)_3]_2$	112	2.2	58 ± 3	1.7 ± 0.1
$^{\bullet}Mn(CO)_3[P(i\text{-}Bu)_3]_2$	110	2.2	57 ± 3	1.7 ± 0.1
$^{\bullet}Mn(CO)_3[P(i\text{-}Pr)_3]_2$	108	2.1	58 ± 3	1.7 ± 0.1
$^{\bullet}Mn(CO)_3[P(O\text{-}i\text{-}Pr)_3]_2$	124	2.5	70 ± 4	2.1 ± 0.1

density in the manganese 4s orbital was estimated from the upper limit values of $A_{iso_{Mn,direct}}$ given in Table VIII and Morton and Preston's[42] calculated value for the isotropic hyperfine coupling constant, $A°_{Mn}$ = 5036 MHz, for an electron totally in a manganese 4s orbital of the $4s3d^n$ configuration. The percentage of unpaired spin density in the manganese 4s orbital is given in eq 10.

$$\% \text{ 4s character} = \frac{A_{iso_{Mn,direct}}}{A°_{Mn}} \times 100 \qquad (10)$$

The results of this calculation are summarized in Table VIII. The unpaired spin density in the manganese 4s orbital has an upper limit of 3%. Consequently, a model of these systems with the unpaired spin occupying a manganese $3d_{z^2}$ orbital is a reasonable approximation. The unpaired spin density located on the ligand phosphorus atoms may also be approximated. The computer-simulated phosphorus superhyperfine values were obtained under the assumption that the **g**, $\mathbf{A}_{Mn}$, and $\mathbf{A}_P$ all had coincident axis systems. Consequently, our parameters may understate the local anisotropy in the phosphorus superhyperfine interaction. Increased local anisotropy in this interaction would reflect an increase in the unpaired spin density in the phosphorus 3p orbitals as well as in the phosphorus 3d orbitals. Because there are no inner loops of electron density for the 3d subshell and one and two inner loops for the 3p and 3s subshells, respectively, the value of $\langle r_{3d}^{-3} \rangle$ is expected to be much smaller than the values of $\langle r_{3p}^{-3} \rangle$ and $\langle r_{3s}^{-3} \rangle$. Therefore, the unpaired spin density in the phosphorus 3d orbitals is probably much less effective than in the phosphorus 3s and 3p orbitals in producing observable hyperfine effects. In addition, the 3d orbitals are expected to be more diffuse than either the 3s or 3p orbitals and thus to have less unpaired spin density per unit volume.

Consequently, we assumed that most of the unpaired spin density on the phosphorus ligands is in $3sp^3$ hybrid orbitals. Using one-fourth of Morton and Preston's[42] $A°_P$ value as the value for the total occupancy in a $3sp^3$ hybrid orbital, one can estimate the percentage of unpaired spin density on each phosphorus ligand.

$$\% \text{ } 3sp^3 \text{ (phosphorus)} = \frac{A_{iso_P}}{A°_{sp^3,P}} \times 100 \qquad (11)$$

These calculated percentages are summarized in Table VIII. As expected, more unpaired spin density is calculated on the phosphite ligand (2.1% per ligand) than on the tertiary phosphine ligands (1.7% per ligand). That the unpaired spin density on the phosphorus ligands is computed to be small for all of the $^{\bullet}Mn(CO)_3L_2$ systems is consistent with our premise that these are primarily localized manganese-centered radical species. The total calculated amount of unpaired spin density delocalized on the phosphorus ligands is about 3.4% in the tertiary phosphine systems and about 4.2% in the phosphite system.

Conclusions

Deciding whether or not this metal-centered model of these $^{\bullet}Mn(CO)_3L_2$ systems is reasonable is of major importance. The amount of unpaired spin density delocalized onto the carbonyl ligands must be larger in the $^{\bullet}Mn(CO)_3L_2$ radicals than in the $^{\bullet}Mn(CO)_5$ radical to account reasonably for all of the unpaired spin density. EPR studies of ^{13}C-labeled $^{\bullet}Mn(CO)_3L_2$ and $^{\bullet}Mn(CO)_5$ would test this assumption. The carbonyl infrared bands obtained for all of the $Mn(CO)_3L_2$ systems[9] are lower in frequency than those for $^{\bullet}Mn(CO)_5$, suggesting a greater degree of metal-to-carbonyl π-bonding. The net effect of the phosphorus ligands in $Mn(CO)_3L_2$ is to supply electron density through the manganese center to the carbonyl ligands. Because there are fewer carbonyl ligands present in the $^{\bullet}Mn(CO)_3L_2$ systems than in $^{\bullet}Mn(CO)_5$, there is more unpaired spin density available to each remaining carbonyl ligand. In the phosphite system, $^{\bullet}Mn(CO)_3[P(O\text{-}i\text{-}Pr)_3]_2$, the unpaired spin density on the carbonyl ligands may be between that in the tertiary phosphine $^{\bullet}Mn(CO)_3L_2$ radical systems and in the $^{\bullet}Mn(CO)_5$ radical system, on the basis of infrared data.[9,43] Such an explanation accounts for the observed infrared data as well as the relatively constant amount of unpaired spin density in the $3d_{z^2}$ orbital in all of the manganese radical species. At least 90% of the unpaired spin density can be accounted for by assuming that each carbonyl ligand carries more unpaired spin density in the substituted $^{\bullet}Mn(CO)_3L_2$ systems than in $^{\bullet}Mn(CO)_5$.

Because all of these $^{\bullet}Mn(CO)_3L_2$ systems give extremely complicated EPR spectra, refining the computer simulations any further is not feasible, given conventional EPR and low-frequency EPR spectroscopy. In polyoriented systems, such as the $^{\bullet}Mn(CO)_3L_2$ frozen solutions, the many orientations represented in the middle region of the spectra produce overlapping features that are difficult to disentangle. Since, at X-band and lower frequencies, the perpendicular features occur in that part of the EPR spectrum in all of the $^{\bullet}Mn(CO)_3L_2$ systems, the perpendicular region is exceedingly difficult to analyze in detail. As mentioned earlier, Q-band (35 GHz) EPR spectra were obtained as part of this study in an attempt to separate features according to the canonical axes of their **g** matrices. Unfortunately, at this frequency *g* strain broadened the lines too much to obtain resolvable and thus useful EPR spectra. ENDOR experiments at frequencies above X-band might further enhance the information obtained from conventional EPR experiments by narrowing spectral lines.

Acknowledgment. Support was provided by the National Science Foundation (NSF Grants CHE-83-12331 and CHE-80-20443) and the National Institutes of Health, Division of Research Resources (NIH Grant RR01811). We thank Drs. James S. Hyde, C. C. Felix, W. E. Antholine, and W. Froncisz for consultation and use of the facilities at the National Biomedical ESR Center, Milwaukee, WI, supported by NIH Grant RR01008.

Registry No. $^{\bullet}Mn(CO)_3[P(n\text{-}Bu)_3]_2$, 67551-64-8; $^{\bullet}Mn(CO)_3[P(i\text{-}Bu)_3]_2$, 81971-50-8; $^{\bullet}Mn(CO)_3[P(i\text{-}Pr)_3]_2$, 83634-20-2; $^{\bullet}Mn(CO)_3[P(O\text{-}i\text{-}Pr)_3]_2$, 83634-19-9.